The Astrophysical Journal, 758:118 (6pp), 2012 October 20 doi:10.1088/0004-637X/758/2/118

DETERMINATION OF THE HELIOSPHERIC RADIAL MAGNETIC FIELD FROM THE STANDOFF DISTANCE OF A CME-DRIVEN SHOCK OBSERVED BY THE *STEREO* SPACECRAFT

Watanachak Poomvises[1,2], Nat Gopalswamy[1], Seiji Yashiro[1,2], Ryun-Young Kwon[1,2], and Oscar Olmedo[3,4]
[1] NASA GSFC, Greenbelt, MD 20771, USA
[2] Department of Physics, Institute for Astrophysics & Computational Sciences, The Catholic University of America, Washington, DC 20064, USA
[3] Space Science Division, U.S. Naval Research Laboratory, Washington, DC 20375, USA
[4] NRC Research at U.S. Naval Research Laboratory, Washington, DC 20375, USA
Received 2012 July 3; accepted 2012 August 26; published 2012 October 8

ABSTRACT

We report on the determination of radial magnetic field strength in the heliocentric distance range from 6 to 120 solar radii ($R_\odot$) using data from Coronagraph 2 (COR2) and Heliospheric Imager I (HI1) instruments on board the *Solar Terrestrial Relations Observatory* spacecraft following the standoff-distance method of Gopalswamy & Yashiro. We measured the shock standoff distance of the 2008 April 5 coronal mass ejection (CME) and determined the flux-rope curvature by fitting the three-dimensional shape of the CME using the Graduated Cylindrical Shell model. The radial magnetic field strength is computed from the Alfvén speed and the density of the ambient medium. We also compare the derived magnetic field strength with in situ measurements made by the *Helios* spacecraft, which measured the magnetic field at the heliocentric distance range from 60 to 215 $R_\odot$. We found that the radial magnetic field strength decreases from 28 mG at 6 $R_\odot$ to 0.17 mG at 120 $R_\odot$. In addition, we found that the radial profile can be described by a power law.

Key words: coronal mass ejections (CMEs) – solar-terrestrial relations

Online-only material: color figures

1. INTRODUCTION

Direct measurement of coronal magnetic fields has been possible only beyond a heliocentric distance of 0.3 AU by the *Helios* mission (Schwenn & Marsch 1990). Future missions such as *Solar Orbiter* and *Solar Probe Plus* are expected to make in situ observation much closer to the Sun. But for now, we only have limited possibilities to measure the coronal magnetic fields close to the Sun.

There have been several reports on coronal magnetic field in the past. For example, Lin et al. (2000) measured the field strength using an infrared spectropolarimeter to observe the strong near-infrared coronal emission line above two active regions and found the field strengths of 33 and 10 G at heights of 0.12 $R_\odot$ and 0.15 $R_\odot$, respectively. Cho et al. (2007) used type II radio burst observations to determine the magnetic field in the lower corona (1.5–2.0 $R_\odot$) to be in the range 1.3–0.4 G. Faraday rotation measurements have also been used to estimate the coronal magnetic field strengths within 10 $R_\odot$; for example, Pätzold et al. (1987) found that the coronal magnetic field at 5 $R_\odot$ is around 100 ± 50 mG, Spangler (2005) found a value of 39 mG at 6.2 $R_\odot$, and Ingleby et al. (2007) found that the coronal magnetic field could be 46–120 mG at 5 $R_\odot$, in agreement with previous studies.

Gopalswamy & Yashiro (2011) and Gopalswamy et al. (2012) reported a new technique to measure the coronal magnetic field strength using the relationship between the shock standoff distance and the Alfvén Mach number of the ambient medium. They obtained the Alfvén speed using the ambient solar wind speed, the shock speed obtained from the height-time measurements, and the derived Mach number. The coronal magnetic field was then obtained by estimating the ambient electron density using the band-splitting information of type II radio bursts or coronagraphic images. Kim et al. (2012) performed a statistical study of the coronal magnetic field strength by applying the technique developed by Gopalswamy & Yashiro (2011) to 10 limb coronal mass ejection (CME) events seen within the Large Angle and Spectrometric Coronagraph (LASCO) field of view (FOV). In the present study, we apply this technique to determine the heliospheric radial magnetic field using data from the *Solar Terrestrial Relations Observatory* (*STEREO*) spacecraft out to 0.5 AU. We also compare the derived radial magnetic field with the in situ measurements made by the *Helios* spacecraft.

In a recent paper, Maloney & Gallagher (2011) reported on the 2008 April 5 CME propagating through interplanetary space from 8 to 120 $R_\odot$ using observations from *STEREO* and studied the standoff distance of the shock ahead of the CME. In this study, we also measure the standoff distance and find that our result is comparable to that of Maloney & Gallagher (2011). In addition, we use the measurements to estimate the heliospheric radial magnetic field strength. A brief description of the standoff-distance measurement of the 2008 April 5 CME is presented in Section 2. The methodology for computing ambient magnetic field and the results are presented in Section 3. Finally, discussion and conclusions are presented in Section 4.

2. OBSERVATION AND MEASUREMENT

For this study, we use data from *STEREO* (Kaiser et al. 2008) and from the *Solar and Heliospheric Observatory* (*SOHO*). The *STEREO* mission is composed of two identical spacecraft that orbit the Sun on approximately the same orbit as the Earth where one satellite is ahead (*A*) and the other is behind (*B*) the Earth. The *STEREO* spacecraft were separated by 48° from each other on 2008 April 5. From two vantage points, the *STEREO* coronagraphs can provide the true propagation of CMEs in three dimensionals (3D) through interplanetary space free of projection effects. The 2008 April 5 CME is clearly observed by the Coronagraph 2 (COR2) and Heliospheric Imager I (HI1) of the Sun Earth Connection Coronal and Heliospheric Investigation (SECCHI; Howard et al. 2008) suite of instruments

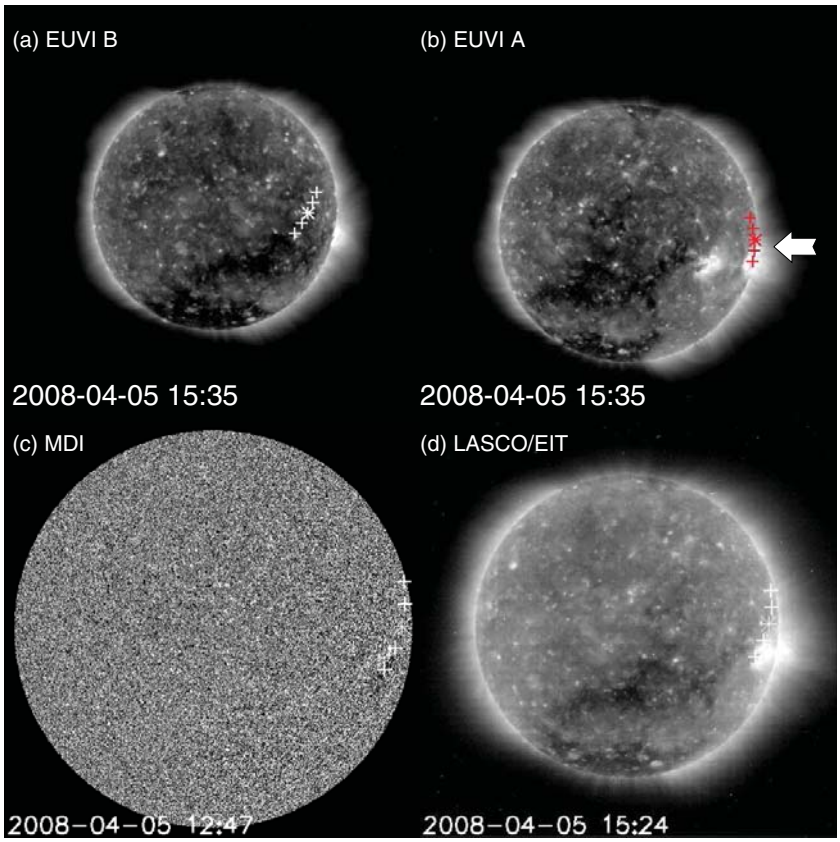

Figure 1. Source region of the 2008 April 5 CME as observed by (a) EUVI B, (b) EUVI A, (c) *SOHO*/MDI, and (d) LASCO/EIT. The central location of the source region is indicated by the asterisk symbol (red color in *STEREO A* represents the frontside origin, while the white color in *STEREO B* represents the backside origin). The plus symbols indicate the footpoints of the CME. An arrow sign in (b) points to the source region of the CME.

(A color version of this figure is available in the online journal.)

on board *STEREO*. Additionally, the Extreme Ultraviolet Imager (EUVI), also part of the SECCHI suite, the Michelson Doppler Image (MDI), and the Extreme-ultraviolet Imaging Telescope (EIT; Delaboudinière et al. 1995) on board *SOHO* are used to locate the source of the CME on the solar surface.

The first sign of activity of this event was seen on the west limb of EUVI A at 15:35 UT. Figure 1 shows the solar disk at this time as observed by EUVI A, EUVI B, MDI, and EIT. Figure 2 shows that the CME can be seen as a flux rope surrounded by a shock in the coronagraphic images (Vourlidas et al. 2003; Ontiveros & Vourlidas 2009; Gopalswamy et al. 2009, 2012; Gopalswamy & Yashiro 2011), most notably seen in COR2 A and COR2 B observations.

The Graduated Cylindrical Shell (GCS) model, developed by Thernisien et al. (2006, 2009), is a tool to model and measure the radial propagation of CMEs free of projection effects. This model describes a CME as a 3D flux rope composed of a semi-circular section forming the body connected to two legs anchored at the Sun. We can get the 3D position of the CME by projecting the GCS model to *STEREO A* and *B* coronagraph images. We measure both the leading edge (LE) of the CME and shock front (R_{sh}) using this model. Note that when we fit the model to the shock the measurement is from the center of the Sun to the shock front. We acknowledge that the geometry of the shock front may not be similar to the flux rope. However, we are only interested in measuring the shock standoff distance, which is the difference between the shock radial distance and the CME LE. Since the view from the two *STEREO* vantage points is different, it is possible to constrain the parameters of the model by manually varying them until the model best approximates the image of the CME in the distinct FOV of each of the instruments simultaneously. The resulting structure is then taken to approximate the true 3D geometrical shape of the CME and to provide information on the radial direction of the CME.

Figure 2 shows the 2008 April 5 CME with the model flux rope overlaid on the observations. The flux rope, as defined by GCS, is projected into the FOV of each of the instruments and drawn as a wire frame (in red). Initially while the CME is a few solar radii from the Sun, we use COR2 images to constrain the CME LE and other parameters of the model (tilt angle, half-angle, and the aspect ratio). In HI1, we usually adjust only the height (LE of CME and shock front), while keeping all other parameters the same as in the last measurement made with COR2. Since the CME originated on the west limb, it appeared in HI1 B images only and was absent in HI1 A, which is expected from the CME trajectory. Additionally, the arrow signs in Figures 2(a), (c), and (d) indicate the shock front ahead of the CME. Figures 2(b) and (e) show the CME in the LASCO/C2 and LASCO/C3 FOV, which are also used to constrain the trajectory of the CME. To better constrain the latitude and longitude, we project the legs of the flux rope back onto the solar surface. The location of two legs is indicated by pairs of plus (+) symbols separated by an asterisk (∗) symbol in Figure 1. The red color on EUVI A represents that the legs are toward the frontside, while the white color in the other observations represents the backside. For example, the symbols that appear as white in the EUVI B image indicate that the projected footpoints of the legs are in fact on the backside from that vantage point.

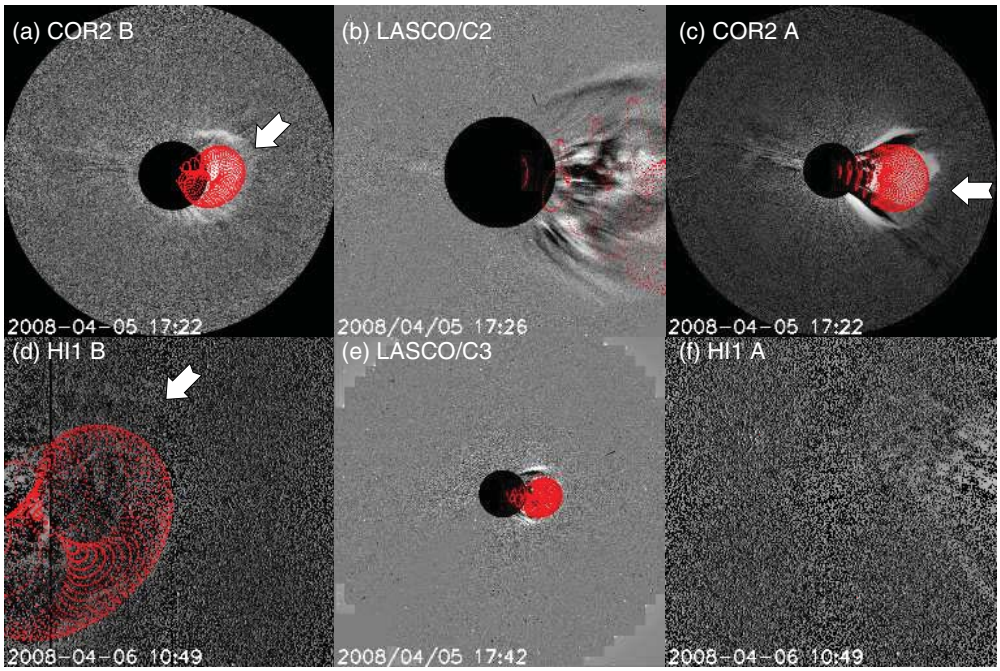

Figure 2. Flux-rope-model measurements (red wire lines) overlaid on the observed images (gray scale) for the 2008 April 5 CME from (a) COR2 B, (b) LASCO/C2, (c) COR2 A, (d) HI1 B, (e) LASCO/C3, and (f) HI1 A. Since the 2008 April 5 CME was originated on the west limb, it appeared in HI1 B images only (absent in HI1 A) as expected from the geometric projection. Additionally, the arrow signs in (a), (c), and (d) indicate the shock front ahead of the CME. The LASCO/C2 and LASCO/C3 images are used in addition to COR2 to constrain the trajectory of the CME.

(A color version of this figure is available in the online journal.)

Figure 3(a) shows the height-time measurements of the CME LE (black) and shock front (red). The first three points in the height-time plot came from COR2, and the remaining from HI1. The values of uncertainty in the height-time plot for the LE and shock front are approximated as 0.12 $R_\odot$ in COR2 and 1.0 $R_\odot$ in HI1 (Cheng et al. 2010), respectively. This uncertainty corresponds to about 8 pixels in both COR2 and HI1 images. We believe that this is a conservative estimation for events with shapes of sharp contrast, but a reasonable one for more diffusive events. Figure 3(b) compares the CME LE (black) and shock front (red) from our measurement with the CME LE (green diamond) and shock front (blue triangle) from Maloney & Gallagher (2011). These results show that the measurement from the GCS model is ∼5% higher than Maloney & Gallagher (2011) for the shock front and approximately ∼6% for the CME LE. The last panel (Figure 3(c)) shows that the standoff distance from Maloney & Gallagher (2011) is ∼12% smaller than our result (GCS model).

3. ANALYSIS AND RESULTS

Gopalswamy & Yashiro (2011) used the relation between the ratio of shock standoff distance ($\triangle$) to the CME radius of curvature (R_C), the adiabatic index (γ), and the Mach number (M) to determine the magnetic field. This relation was originally applied to in situ (one-dimensional) observations of interplanetary CMEs by Russell & Mulligan (2002) and later applied to remote sensing (two-dimensional) observations used by Gopalswamy & Yashiro (2011) and Gopalswamy et al. (2012). The relation is

$$\frac{\triangle}{R_C} = \frac{0.81[(\gamma-1)M^2+2]}{[(\gamma+1)(M^2-1)]}. \quad (1)$$

The standoff distance ($\triangle$) is calculated from the distance of the shock front ($R_{\rm sh}$) minus the distance of CME LE. The variation of standoff distance might be large at the legs of the flux rope. However, in this work, we measured the distance between the shock nose and the CME LE as the standoff distance. We also calculated the propagation of the error in standoff distance from the height of the CME and the distance of the shock. We assume that the value of the adiabatic index could be either 4/3 or 5/3. The radius of curvature (R_C) is calculated from the flux-rope geometry of the GCS model (Thernisien 2011). For the CME observed in COR2 at 17:22 UT, the LE of the CME is 9.00 $R_\odot$, $R_{\rm sh}$ = 12.51 $R_\odot$, and $\triangle/R_C = 0.47$, which gives $M = 1.81 \pm 0.004$ for $\gamma = 4/3$ and $M = 2.00 \pm 0.06$ for $\gamma = 5/3$. In HI 1 at 10:49 UT, the LE of the CME is 103.07 $R_\odot$, $R_{\rm sh}$ = 121.83 $R_\odot$, and $\triangle/R_C = 0.22$, which gives $M = 2.97 \pm 0.01$ for $\gamma = 4/3$ and $M = 7.12 \pm 0.12$ for $\gamma = 5/3$. We calculated the error in the Mach number, which is around 2% for $\gamma = 4/3$ and 10% for $\gamma = 5/3$. From Equation (1), we simply derive

$$M^2 = \frac{(1.62 + R\gamma + R)}{(R(\gamma+1) - 0.81(\gamma-1))}; \quad R = \frac{\triangle}{R_C}. \quad (2)$$

When we change $\gamma = 4/3$ to 5/3 in Equation (2), we see that the $0.81(\gamma-1)$ term is close to $R(\gamma+1)$. Then, the Mach number for $\gamma = 5/3$ is larger than that for $\gamma = 4/3$, resulting in a higher error for the $\gamma = 5/3$ case. This problem was discussed in Kim et al. (2012).

The Alfvén velocity (V_A) is related to the solar wind speed ($V_{\rm sw}$), the shock velocity ($V_{\rm sh}$), and Mach number (M) by

$$V_A = \frac{(V_{\rm sh} - V_{\rm sw})}{M}. \quad (3)$$

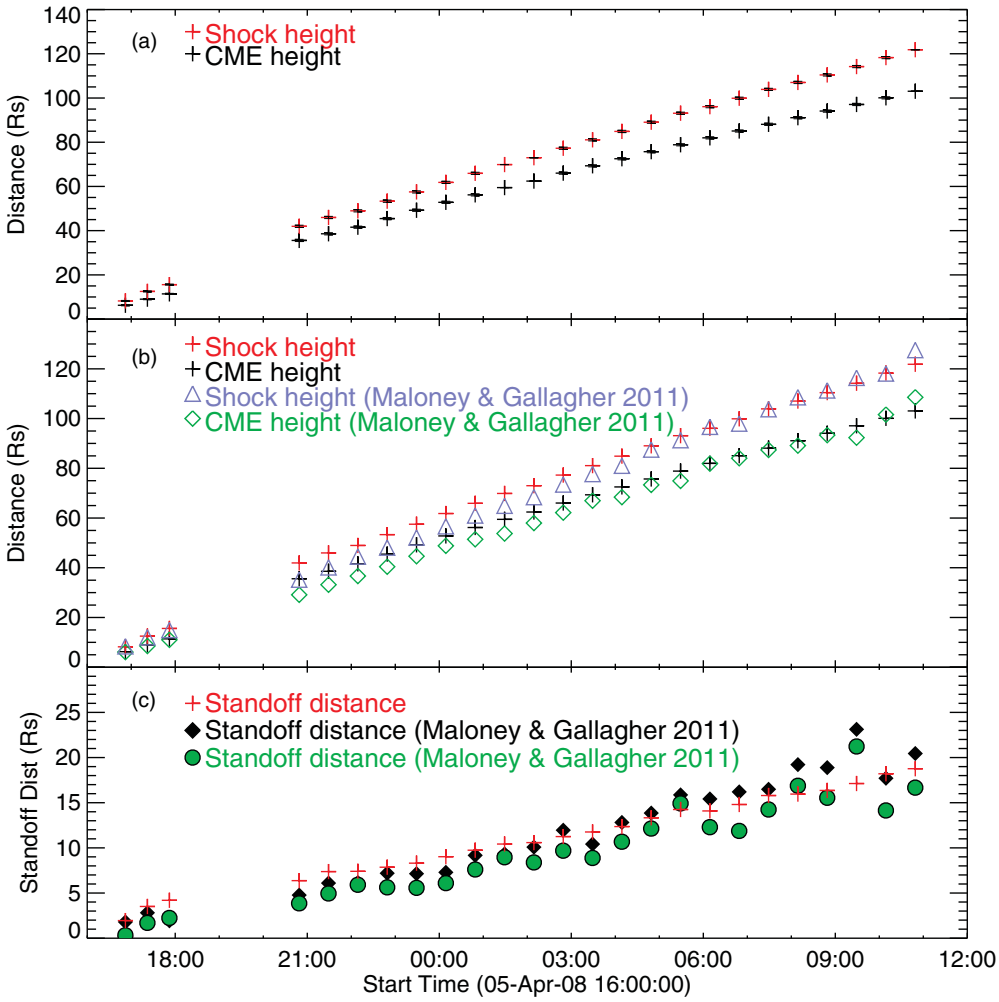

Figure 3. Height-time plots and standoff distance of the 2008 April 5 event. (a) Height-time plot of the CME leading edge (black) and the shock front (red). (b) The CME leading edge (black) and shock front (red) from our measurement in comparison with the CME leading edge (green diamond) and shock front (blue triangle) from Maloney & Gallagher (2011). These results show that the measurement from the GCS model is ∼5% higher than Maloney & Gallagher (2011) for the shock front and ∼6% for the CME leading edge. (c) Comparison of the standoff distance from the GCS geometry and Maloney & Gallagher (2011); the latter is ∼12% smaller than the GCS value.

(A color version of this figure is available in the online journal.)

The shock velocity is derived from the height-time measurements. We use the Sheeley et al. (1997) solar wind profile,

$$V_{\rm sw}^2 = 1.75 \times 10^5 [1 - e^{(-(r-4.5))/15.2}]. \quad (4)$$

With this equation it is found that at $R_{\rm sh} = 12.51\ R_\odot$, $V_{\rm sw} = 418.32$ km s^{-1} for $\gamma = 4/3$ and $V_A = 558$ km s^{-1} for $\gamma = 5/3$. For $R_{\rm sh} = 121.83\ R_\odot$, $V_{\rm sw} = 418.33$ km s^{-1}, $V_A = 180$ km s^{-1} for $\gamma = 4/3$, and $V_A = 80$ km s^{-1} for $\gamma = 5/3$.

The solar software routine "pb_ inverter.pro" provides the average density from LASCO/C2 and LASCO/C3 polarized brightness images, so we can determine the multipliers to the density models of Leblanc et al. (1998, LDB) and Saito et al. (1977, SMP) as was done by Gopalswamy & Yashiro (2011):

$$n(r) = 1.36 \times 10^6 r^{-2.14} + 1.68 \times 10^8 r^{-6.13} \quad (5)$$

$$n(r) = 3.3 \times 10^5 r^{-2} + 4.1 \times 10^6 r^{-4} + 8.0 \times 10^7 r^{-6}. \quad (6)$$

The density range is 0.58 $\times 10^3$ cm^{-3} to 0.72 $\times 10^3$ cm^{-3} and 1.36 $\times 10^3$ cm^{-3} to 1.72 $\times 10^3$ cm^{-3} for Saito et al. (1977) and Leblanc et al. (1998), respectively. So, the average for the LDB density model is 1.54 $\times 10^3$ cm^{-3} in Equation (5) and 0.65 $\times$ 10^3 cm^{-3} for the SMP model with Equation (6).

The ambient magnetic field strength (B) is calculated from

$$B = 4.58 \times 10^{-7} V_A n^{1/2}, \quad (7)$$

where n is the upstream plasma density in cm^{-3} and B is in G. Substituting for n and V_A in Equation (7), we get the ambient magnetic field strength in the distance range from 0.02 to 0.5 AU as 32.56–0.48 mG and 27.76–0.20 mG for the LDB density model using either $\gamma = 4/3$ or $\gamma = 5/3$, respectively. For the SMP density model, the ambient magnetic field is similar to the LDB model; it is 33.77–0.45 mG for $\gamma = 4/3$ and 28.79–0.19 mG for $\gamma = 5/3$. We can get the radial component of the magnetic field (B_r) from the calculated magnetic field strength using the relation

$$B = B_r \sqrt{1 + \left(\frac{\Omega r}{v_{\rm sw}}\right)^2}. \quad (8)$$

Here, B is the measured magnetic field strength, r is the heliocentric distance in AU, B_r is the radial magnetic field at

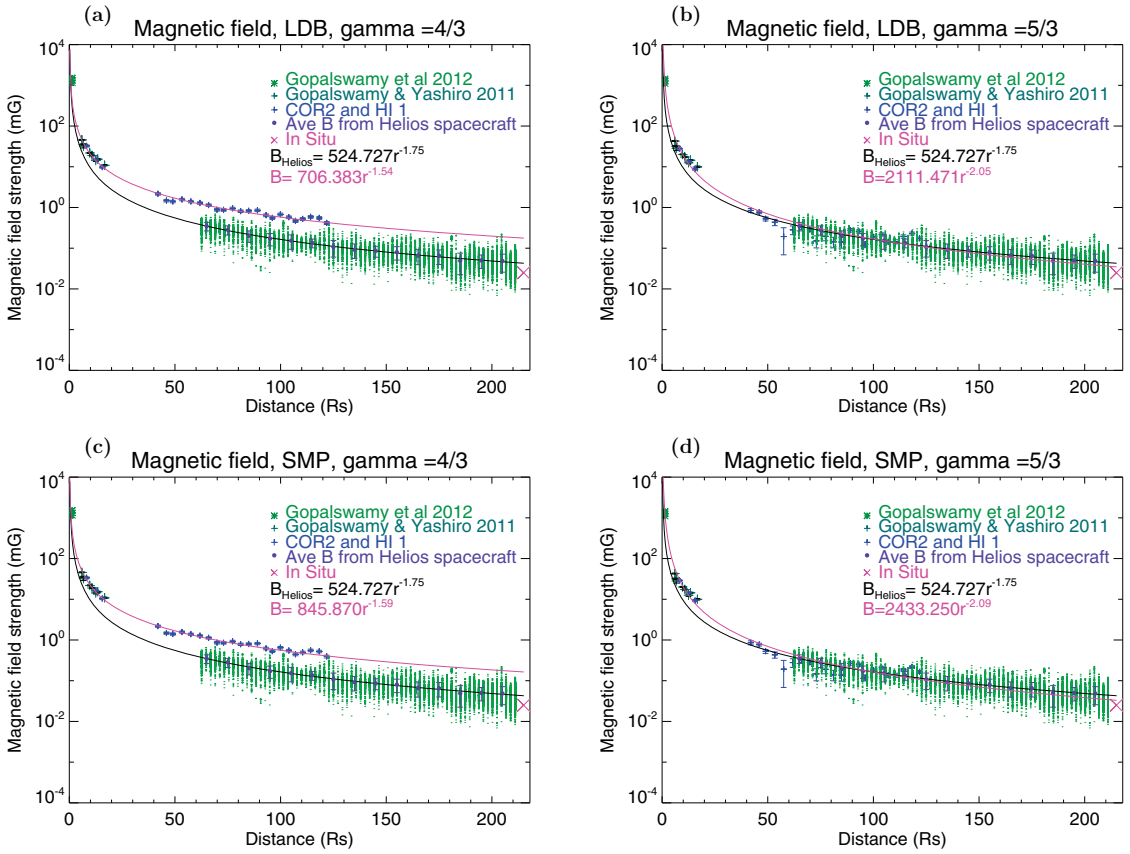

Figure 4. Radial magnetic field strength from *STEREO* spacecraft and the fitting profile of the magnetic field for the density profile by Leblanc et al. (1998, LDB) with $\gamma = 4/3$(a) and 5/3(b) and the Saito et al. (1977, SMP) density profile with $\gamma = 4/3$ (c) and 5/3 (d). The pink line in the radial magnetic field plots shows the functional fitting with the calculated magnetic field from 6 to 120 R_s. The first three data points in this plot are from Gopalswamy et al. (2012), using the *Solar Dynamics Observatory* (*SDO*) to observe the standoff distance from flux rope and shock front. The second group of data points are from Gopalswamy & Yashiro (2011), which correspond to the range from 6 to 23 R_s from LASCO/C2 and *STEREO*/COR2 observation. The light blue plus symbols (+) denote the data from COR 2 and HI 1 from the present work. The green dots show the observational data from *Helios* spacecraft 1 and 2. The blue circles represent the average magnetic field from the *Helios* spacecraft. Finally, the pink cross shows the average magnetic field strength from in situ measurement from *ACE*.

distance r, and Ω is solar angular rotation rate, which is about 2.91×10^{-6} rad s^{-1}. The radial magnetic field strength decreases from 32.45 $\pm$ 1.9 mG to 0.41 $\pm$ 0.03 mG for the LDB model and $\gamma = 4/3$, and for $\gamma = 5/3$ the radial magnetic field is 27.66 $\pm$ 1.6 mG to 0.17 $\pm$ 0.02 mG. For the SMP model, the calculated radial field decreases from 33.64 $\pm$ 1.8 mG to 0.39 $\pm$ 0.03 mG for $\gamma = 4/3$, and for $\gamma = 5/3$ the radial field is 28.69 $\pm$ 1.6 mG to 0.16 $\pm$ 0.013 mG. The error propagates from the error in high-time measurement, the error in the calculated Mach number, the error in shock velocity and Alfvén velocity, and the error in density. The radial magnetic field profile can be described by a power law. For $\gamma = 4/3$, the power law can be written as $B_r = 706.383r^{-1.54}$ and $B_r = 845.870r^{-1.59}$ for the LDB and the SMP models, respectively. For γ =5/3, the power-law index is ~2 and is written as $B_r = 2111.471r^{-2.05}$ and $B_r = 2433.250r^{-2.09}$ for the LDB and the SMP models, respectively.

Figure 4 shows the computed magnetic field from the lower corona to 1 AU. The first three points in this plot are from Gopalswamy et al. (2012), reported using the *Solar Dynamics Observatory* (*SDO*) to observe the standoff distance from the flux rope to the shock front. The dark green asterisks are the data from Gopalswamy & Yashiro (2011), which correspond to the range from 6 to 23 $R_\odot$ using LASCO/C2 and *STEREO*/COR2 observations. The blue plus symbols (+) denote the data from COR 2 and HI 1 from the present work. The green dots show the observational data from *Helios* spacecraft 1 and 2. The solid blue circles represent the average magnetic field from the *Helios* spacecraft. Finally, the pink cross shows the average magnetic field strength from in situ measurements from the *Advanced Composition Explorer* (*ACE*). The top row shows the magnetic field obtained using the density profile from Leblanc et al. (1998). The second row shows the magnetic field from the Saito et al. (1977) density profile. The right column in Figure 4 shows that the radial magnetic field strength fits well with all the observational data and also fits both density models with $\gamma = 5/3$.

When we used $\gamma = 4/3$ and 5/3 and kept the CME velocity, the shock velocity, the curvature of the flux rope, and the density from the profiles constant, we found that the calculated magnetic field profile is higher than the those observed with the *Helios* spacecraft and *ACE* at 1 AU for $\gamma = 4/3$. We note that when γ changes, the Mach number becomes smaller. The Alfvén speed is then larger and will increase the calculated radial magnetic field, which will therefore not match the in situ observation. This result suggests that $\gamma = 5/3$ may be more appropriate than $\gamma = 4/3$.

4. DISCUSSION AND CONCLUSIONS

We obtained the heliospheric radial magnetic field derived from the standoff distance of a CME-driven shock to heliocentric

distances larger than any previous study and compared the result with in situ spacecraft measurements. Using the technique developed by Gopalswamy & Yashiro (2011) and Gopalswamy et al. (2012), we are able to calculate the radial magnetic field using data from the *STEREO* spacecraft out to heliocentric distances from 6 to 120 $R_{\odot}$ (0.02–0.5 AU), and the radial magnetic field strength decreases from 27.66 to 0.17 mG, respectively.

The advantage of the circular fitting to the flux rope is that it approximates the radial width of a flux rope as the curvature of a circle. However, the radial width suddenly increases in the low corona ($R_{\odot} < 5$), and a circle might not fit well the morphology of a flux rope in the high corona because of the drag and Lorentz force acting on it (Chen 1996; Cargill 2004; Poomvises et al. 2010) and causing it to deform. In other words, in the low corona the curvature of a flux rope can be described by the radius of a circle, but as the flux rope propagates and expands further heliosphere, the curvature will increase rapidly (Gopalswamy et al. 2012) and a circle may not be appropriate. Furthermore, the circular fitting method only provides the projected curvature of the flux rope in the FOV of the instrument. In this study we applied the circular fitting method to calculate the curvature of the flux rope but found that the curvature was underestimated. We came to this conclusion when we compared our calculation of the radial magnetic field with in situ observations made with *Helios* and *ACE*. For this reason we applied the GCS model to estimate the curvature of the flux rope free of projection effects and found a better comparison of the calculation of the radial magnetic field with in situ measurements.

In conclusion, the radial magnetic field profile can be described by a power law with an index of ~ 2, in agreement with the magnetic field measurements from the *Helios* and *ACE* spacecraft. The computed radial magnetic field from the stand-off distance of the CME-driven shock agrees with the *Helios* spacecraft data for an adiabatic index of $5/3$. These results verify that these techniques can derive the radial magnetic field to larger distances from the Sun. We note that the adiabatic index plays an important role in the calculation of the radial magnetic field strength because increasing γ will increase the Mach number and decrease the Alfvén velocity, therefore decreasing the radial magnetic field. In the future, *Solar Orbiter* and *Solar Probe Plus* will provide more information on the magnetic field close to the Sun and can provide validation for the approach presented. But for now, this technique is a useful tool in calculating the magnetic field close to the Sun up to 0.5 AU.

This research is supported by NASA LWS TR&T.

REFERENCES

Cagill, P. 2004, Sol. Phys., 221, 135
Chen, J. 1996, J. Geophys. Res., 101, 27499
Cheng, X., Zhang, J., Ding, M. D., & Poomvises, W. 2010, ApJ, 712, 752
Cho, K.-S., Lee, J., Gary, D. E., Moon, Y.-J., & Park, Y. D. 2007, ApJ, 665, 799
Delaboudinière, J.-P., Artzner, G. E., Brunaud, J., et al. 1995, Sol. Phys., 162, 291
Gopalswamy, N., Nitta, N., Akiyama, S., Mäkelä, P., & Yashiro, S. 2011, ApJ, 744, 72
Gopalswamy, N., Thompson, W. T., Davila, J. M., et al. 2009, Sol. Phys., 259, 227
Gopalswamy, N., & Yashiro, S. 2011, ApJ, 736, L17
Howard, R. A., Moses, J. D., Vourlidas, A., et al. 2008, Space Sci. Rev., 136, 67
Ingleby, L. D., Spangler, S. R., & Whiting, C. A. 2007, ApJ, 668, 520
Kaiser, M. L., Kucera, T. A., Davila, J. M., et al. 2008, Space Sci. Rev., 136, 5
Kim, R. S., Gopalswamy, N., Moon, Y. J., Cho, K.-S., & Yashiro, S. 2012, ApJ, 746, 118
Leblanc, Y., Dulk, G. A., & Bougeret, J. L. 1998, Sol. Phys., 183, 165
Lin, H., Penn, M. J., & Tomczyk, S. 2000, ApJ, 541, L83
Maloney, A. S., & Gallagher, T. P. 2011, ApJ, 736, L5
Ontiveros, V., & Vourlidas, A. 2009, ApJ, 693, 267
Pätzold, M., Bird, M. K., Volland, H., et al. 1987, Sol. Phys., 109, 91
Poomvises, W., Zhang, J., & Olmedo, O. 2010, ApJ, 717, L159
Russell, C. T., & Mulligan, T. 2002, Planet. Space Sci., 50, 527
Saito, K., Poland, A. I., & Munro, R. H. 1977, Sol. Phys., 55, 121
Schwenn, R., & Marsch, E. 1990, Physics of the Inner Heliosphere Large-Scale Phenomena (Physics and Chemistry in Space, Vol. 20; Berlin: Springer)
Sheeley, N. R., Jr., Wang, Y.-M., Hawley, S. H., et al. 1997, ApJ, 484, 472
Spangler, S. R. 2005, Space Sci. Rev., 121, 189
Thernisien, A. 2011, ApJS, 194, 33
Thernisien, A., Howard, R. A., & Vourlidas, A. 2006, ApJ, 652, 763
Thernisien, A., Vourlidas, A., & Howard, R. A. 2009, Sol. Phys., 256, 111
Vourlidas, A., Wu., S. T., Wang, A. H., Subramanian, P., & Howard, R. A. 2003, ApJ, 598, 1392